Available online at www.sciencedirect.com
SCIENCE DIRECT®
International Journal of Heat and Mass Transfer 49 (2006) 1896–1906
International Journal of HEAT and MASS TRANSFER
www.elsevier.com/locate/ijhmt

Forced convection in a square cavity with inlet and outlet ports

S.M. Saeidi, J.M. Khodadadi *

Mechanical Engineering Department, Auburn University, 201 Ross Hall Auburn, AL 36849-5341, USA

Received 23 March 2005; received in revised form 28 October 2005
Available online 10 January 2006

Abstract

A finite-volume-based computational study of steady laminar forced convection inside a square cavity with inlet and outlet ports is presented. Given a fixed position of the inlet port, the location of the outlet port is varied along the four walls of the cavity. The widths of the ports are equal to 5%, 15% and 25% of the side. By positioning the outlet ports at nine locations on the walls for $Re = 10$, 40, 100 and 500 and $Pr = 5$, a total of 108 cases were studied. For the shortest distance between the inlet and outlet ports along the top wall, a primary clockwise (CW) rotating vortex that covers about 75–88% of the cavity is observed. As the outlet port is lowered along the right wall, the CW primary vortex diminishes in strength, however a counter-clockwise (CCW) vortex that is present next to the top right corner grows in size. With the outlet port moving left along the bottom wall, the CW primary vortex is weakened further and the CCW vortex occupies nearly the right half of the cavity. The pressure drop varies drastically depending on Re and the position of the outlet port. If the outlet port is on the opposite or the same wall as the inlet, the pressure drop is smaller in comparison to a case where it is located on the adjacent walls. The maximum pressure drop occurs when the outlet port is on the left side of the bottom wall and the minimum is achieved where the outlet is on the middle of the right wall. Regions of high temperature gradient are consistently observed at the interface of the throughflow and next to the solid walls on both sides of the outlet port. Local Nusselt numbers are low at three corners when no outlet port is present in their vicinity, whereas intense heat transfer rate is observed on the two sides of the outlet port. Between these minima and maxima, the local Nusselt number can vary drastically depending on the flow and temperature fields. By placing the outlet port with one end at three corners, maximum overall Nusselt number of the cavity can be achieved. Minimum overall heat transfer of the cavity is achieved with the outlet port located at the middle of the walls. The case exhibiting maximum heat transfer and minimum pressure drop is observed when the outlet port is located at dimensionless wall coordinate $(2 + 0.5W)$.

1. Introduction

Forced convection within a lid-driven sealed cavity and buoyancy-driven convection within differentially heated cavities have provided excellent opportunities for researchers to test and benchmark computational tools for solution of complex flows with recirculation. In addition to their geometrical simplicity, both of these flows offer simultaneous existence of diverse flow regimes involving boundary layers and multiple separated regions. To this end, great attention has been focused on these flows and variations of them [1,2]. A logical extension of this work is to concentrate on more complicated flow situations in cavities upon introduction of multiple inlet and outlet ports. These flow systems offer a wide range of interesting flow regimes and have a great number of engineering applications. For instance, mixed convection studies within cavities that contain heat sources [3–6] are of great interest in electronic cooling, ventilation of buildings and design of solar collectors. Simulations of unsteady mixed convection in thermal storage applications have also received a great deal of attention for many decades [7–13]. Other isolated applications related to mass transfer in cavities [14], relaxation tanks employed in petroleum and transformer industries [15], transient removal of contaminated fluid from cavities [16] and food processing [17] are also noteworthy. Design of microfabricated fluid filters [18] and piezoelectric liquid-compatible microvalves [19] can also benefit from the knowledge that is gained from the present study.

* Corresponding author. Tel.: +1 334 844 3333; fax: +1 334 844 3307.
E-mail address: khodajm@auburn.edu (J.M. Khodadadi).

0017-9310/$ - see front matter © 2005 Elsevier Ltd. All rights reserved.
doi:10.1016/j.ijheatmasstransfer.2005.10.033

Nomenclature

Nu	local Nusselt number, defined by Eq. (9)
$\overline{Nu}_{tot}$	total or overall Nusselt number, defined by Eq. (10)
s	coordinate adopted for distance along the walls, m
S	dimensionless coordinate, i.e., $S = s/H$
T_{in}	temperature of the fluid at the inlet port, K
T_w	temperature of the wall, K

Greek symbol

θ	dimensionless temperature, i.e., $(T - T_{in})/(T_w - T_{in})$

Subscripts

b, l, r, t related to the bottom, left, right and top walls

Given the variety of applications sharing the cavity geometry with inlet and outlet ports, the present parametric study was undertaken in order to gain further knowledge of the complicated flow and thermal fields in such a configuration.

2. Problem formulation

The schematic drawing of the system and the coordinates are shown in Fig. 1. The height and width of the cavity are denoted by H and L, respectively. In this study, only a square cavity is considered ($H = L$). The depth of the enclosure perpendicular to the plane of the diagram is assumed to be long. Hence, the problem can be considered to be two-dimensional. The fluid enters the cavity through an inlet port of width w_i that is located on the left vertical wall extending from $y = (H - w_i)$ to $y = H$. An exit port of width w_o can be present on any of the four walls. In this study the widths of the inlet and outlet ports are identical ($w_i = w_o = w$). A special coordinate system (s) along the walls is adopted with its origin at $x = 0$ and $y = H$, as identified by the dashed lines in Fig. 1. The s-coordinates of the symmetry planes of the inlet and outlet ports are $0.5w_i$ and s_o, respectively. The temperature of the fluid entering the cavity is T_{in}, whereas the four solid walls of the cavity are maintained at temperature T_w with $T_w > T_{in}$.

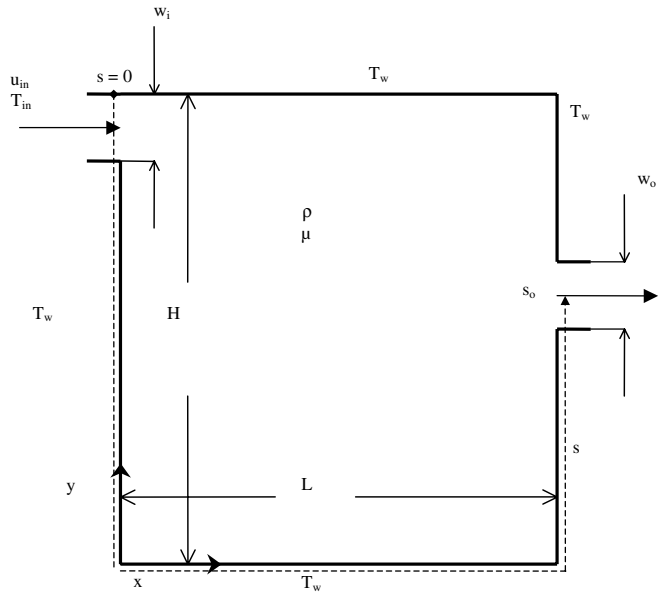

Fig. 1. Schematic diagram of a cavity with inlet and outlet ports.

2.1. Dimensionless form of the governing equations

The flow field is considered to be steady and the fluid is incompressible possessing constant properties. Dimensionless form of the governing equations can be obtained via introducing dimensionless variables. The lengths can be scaled by the cavity length H and the velocities can be scaled by the inlet fluid velocity, u_{in}. As for the temperature, the two extreme values (T_{in} and T_w) are used. The dimensionless variables (capitalized letters and θ) are then defined as

$$X = \frac{x}{H}, \quad Y = \frac{y}{H}, \quad U = \frac{u}{u_{in}}, \quad V = \frac{v}{u_{in}},$$
$$P = \frac{p}{\rho u_{in}^2}, \quad \theta = \frac{T - T_{in}}{T_w - T_{in}}. \tag{1}$$

Variables u, v, p and T are the velocity components in the x-, y-directions, pressure and temperature, respectively. Based on the dimensionless variables above, the dimensionless equations for the conservation of mass, momentum and thermal energy are

$$\frac{\partial U}{\partial X} + \frac{\partial V}{\partial Y} = 0, \tag{2}$$

$$U\frac{\partial U}{\partial X} + V\frac{\partial U}{\partial Y} = -\frac{\partial P}{\partial X} + 2\frac{w}{H}\frac{1}{Re}\left(\frac{\partial^2 U}{\partial X^2} + \frac{\partial^2 U}{\partial Y^2}\right), \tag{3}$$

$$U\frac{\partial V}{\partial X} + V\frac{\partial V}{\partial Y} = -\frac{\partial P}{\partial Y} + 2\frac{w}{H}\frac{1}{Re}\left(\frac{\partial^2 V}{\partial X^2} + \frac{\partial^2 V}{\partial Y^2}\right), \tag{4}$$

$$U\frac{\partial \theta}{\partial X} + V\frac{\partial \theta}{\partial Y} = 2\frac{w}{H}\frac{1}{PrRe}\left(\frac{\partial^2 \theta}{\partial X^2} + \frac{\partial^2 \theta}{\partial Y^2}\right). \tag{5}$$

In the energy equation, the viscous dissipation terms are neglected. The Reynolds number is defined as $Re = u_{in}(2w)/v$ and the Prandtl number is $Pr = v/\alpha$. Quantities α and v are the thermal diffusivity and kinematic viscosity of the fluid, respectively. The Reynolds number signifies the ratio of inertia and viscous forces, whereas the Prandtl

number indicates the ratio of the momentum and thermal diffusivities.

Denoting $W = w/H$, the dimensionless form of the boundary conditions are

$$\text{At the inlet } (X = 0, Y = (1 - W) \text{ to } 1): \quad U = 1, V = 0, \theta = 0, \tag{6}$$

$$\text{On the four solid walls: } \quad U = V = 0, \theta = 1.$$

At the outlet port ($S = s/H = S_o - 0.5W$ to $S_o + 0.5W$), the velocity and temperature fields were taken to be fully developed. The trade-off issues related to using this boundary condition as opposed to attaching an exit duct or prescribing a known constant outflow pressure were studied [20]. From the foregoing formulation, it is clear that the dimensionless parameters governing this problem are Re, Pr, S_o and W. In this study, the Prandtl number of the fluid is fixed to 5. The Reynolds numbers considered are 10, 40, 100 and 500.

2.2. Computational details

The governing equations were iteratively solved by the finite-volume-method using Patankar's SIMPLE algorithm [21]. A two-dimensional uniformly spaced staggered grid system was used. Hayase et al.'s [22] QUICK scheme was utilized for the convective terms, whereas the central difference scheme was used for the diffusive terms. In order to keep consistent accuracy over the entire computational domain, a third-order-accurate boundary condition treatment suggested by Hayase et al. [22] was adopted.

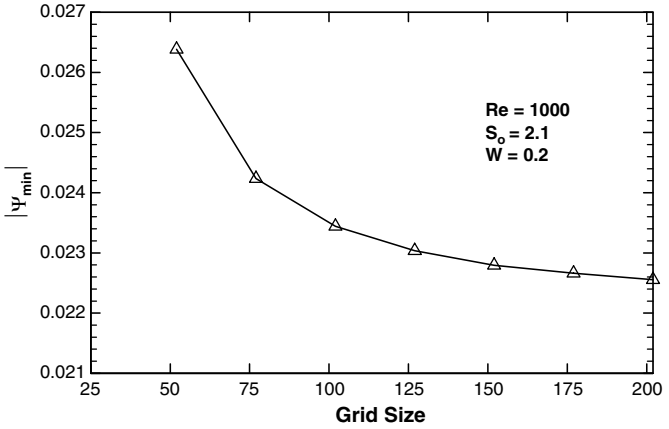

Fig. 2. The absolute value of the stream function at the center of primary vortex, ψ_{min}, as a function of the grid size ($Re = 1000$, $S_o = 2.1$ and $W = 0.2$).

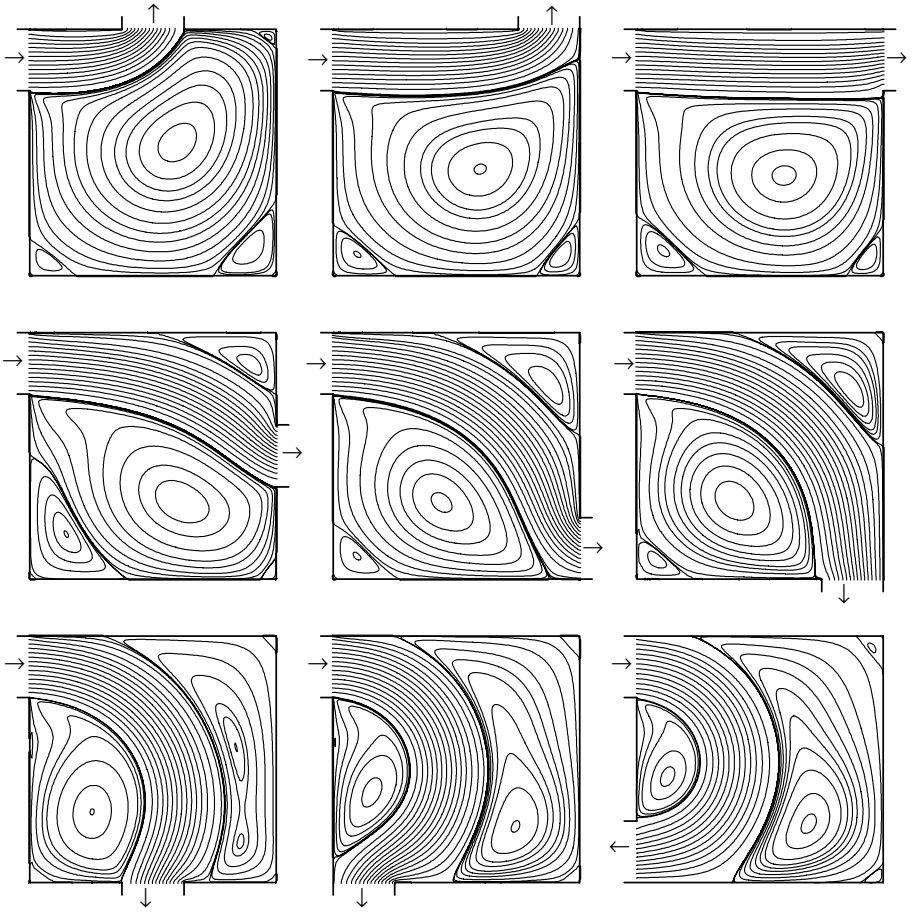

Fig. 3. Streamlines for $Re = 500$ and $W = 0.25$ for nine different positions of the outlet port.

2.3. Grid independence study and benchmarking of the code

In order to determine the proper grid size for this study, a grid independence test was conducted with $Re = 1000$, $S_o = 2.1$ and $W = 0.2$. Seven uniformly spaced grid densities were used for the grid independence study. These grid densities were $50^x \times 50^y$, $75^x \times 75^y$, $100^x \times 100^y$ and $125^x \times 125^y$, $150^x \times 150^y$, $175^x \times 175^y$ and $200^x \times 200^y$. The extreme value of the stream function field that relates to the primary vortex (i.e., ψ_{min}) is commonly used as a sensitivity measure of the accuracy of the solution and was selected as the monitoring variable for the grid independence study. Fig. 2 shows the dependence of the quantity ψ_{min} on the grid size. Considering both the accuracy and the computational time, the following calculations were all performed with a $160^x \times 160^y$ grid system that accommodated resolving all the three widths of the outlet port on the uniform grid system. The code was recently tested and verified extensively [1,2] via comparing the results with established forced and buoyancy-driven convection benchmark problems. In extending the applicability of the code to this problem, extensive benchmarking was undertaken in relation to the backward-facing and forward-facing step problems [20].

2.4. Parameters for numerical simulations

Tolerance of the normalized residuals upon convergence is set to 10^{-6} for most cases, whereas for some high Re cases a less stringent condition (10^{-5}) was imposed. For Re numbers other than 500, the under-relaxation parameters for u, v, and T are all set to 0.6, whereas under-relaxation parameter for pressure correction is set to 0.3. For $Re = 500$, these were set to 0.6, 0.6, 0.2 and 0.3.

3. Results and discussion

In order to understand the flow field and heat transfer characteristics of this problem, a total of 108 cases were considered. This involved studying the effect of placing an outlet port at nine different positions for a fixed position of the inlet port. The Reynolds numbers are 10, 40, 100 and 500. The widths of both ports are equal to 5%, 15% and 25% of the width of the cavity. The typical number of iterations needed to converge was 11,000–60,000. Convergence difficulties were encountered for seven cases with $Re = 500$ and $W = 0.05$ when the outlet port was not located next to the lower right corner. Similar difficulties were also repeated by running these cases on the commercial CFD package FLUENT. For these cases, the hybrid differencing

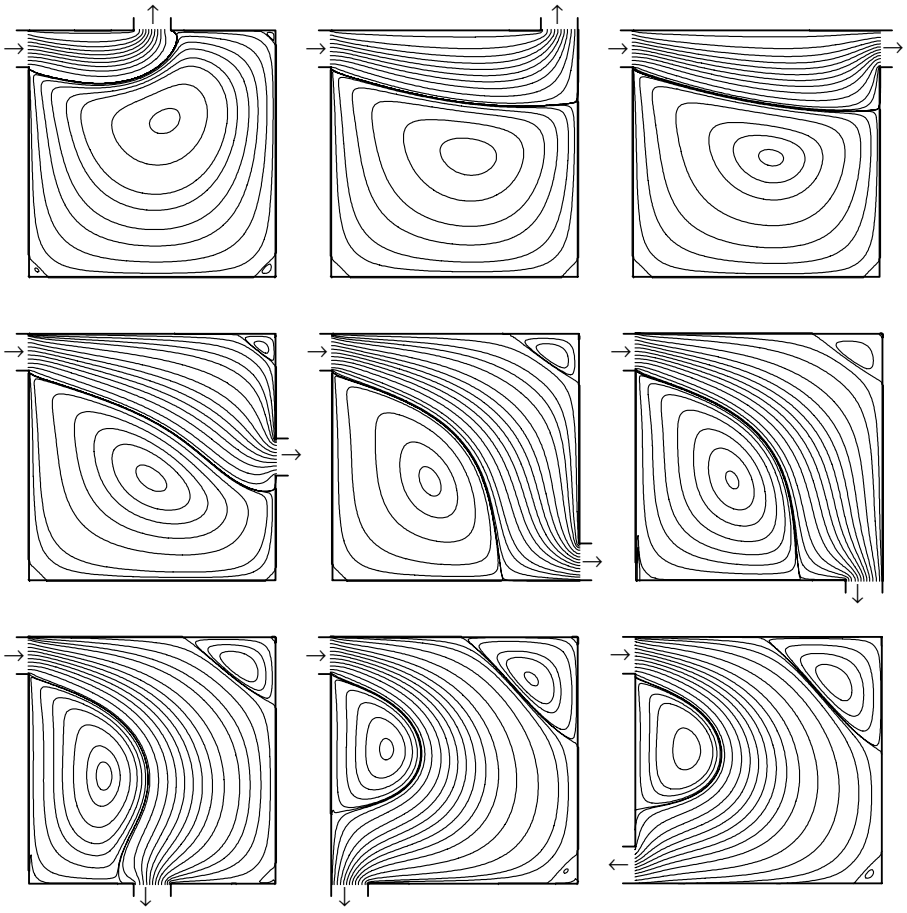

Fig. 4. Streamlines for $Re = 40$ and $W = 0.15$ for nine different positions of the outlet port.

scheme was utilized. All the calculations were performed on a Cray SV1 of the Alabama Supercomputer Center (Huntsville, AL).

3.1. Flow fields in the cavity

The streamlines corresponding to nine cases with $Re = 500$ and $W = 0.25$ are shown in Fig. 3 for different positions of the outlet port. Similar streamline patterns for nine cases with $Re = 40$ and $W = 0.15$ are shown in Fig. 4. For each of the individual cavities shown, two arrows are drawn to help the reader clearly identify the inlet and outlet ports. Nine different positions of the outlet port are shown corresponding to variation of S_o from 0.875 to 3.5 in Fig. 3 and 0.925 to 3.5 in Fig. 4. It is observed that the streamlines representing the throughflow of the incoming fluid (streamline values of zero and inlet mass flowrate) do not coincide with the two ends of the outlet ports. The streamlines for the top row correspond to cases where the outlet port is positioned on the top wall or closest to it. The fresh fluid entering the cavity travels the shortest distance possible before leaving the cavity. For these three cases of Fig. 3, the presence of a primary CW rotating vortex that occupies 75–88% of the cavity is clearly observed. Two CCW rotating vortices that are located at the bottom two corners—but are much smaller that the primary vortex—are the other permanent features of these three cases. Considering similar three positions of the outlet ports, the flow fields appeared very similar for the other Re numbers studied (e.g., the top row of Fig. 4) except for $Re = 10$, with the strength the corner vortices diminishing as Re decreases. For the $Re = 10$ cases corresponding to the same outlet port positions, the cavity was generally dominated by two large CW rotating vortices at the bottom two corners regardless of the width size. For an outlet port located at $S_o = 3.5$ with $Re = 10$, these two vortices merged to form a single CW vortex occupying the bottom of the cavity and a third small CCW vortex was observed at the top right hand corner. Going through the middle row of Fig. 3, one can observe the changes in the flow field as the position of the outlet port is lowered along the right side wall. The area occupied by the CW rotating primary vortex diminishes as the outlet port is lowered. A CCW rotating vortex that is created next to the top right corner covers a larger portion of the cavity as the outlet port is lowered. For the same three positions of the outlet ports, the features of the flow fields were retained for the other Re numbers studied (such as the middle row of Fig. 4). For the

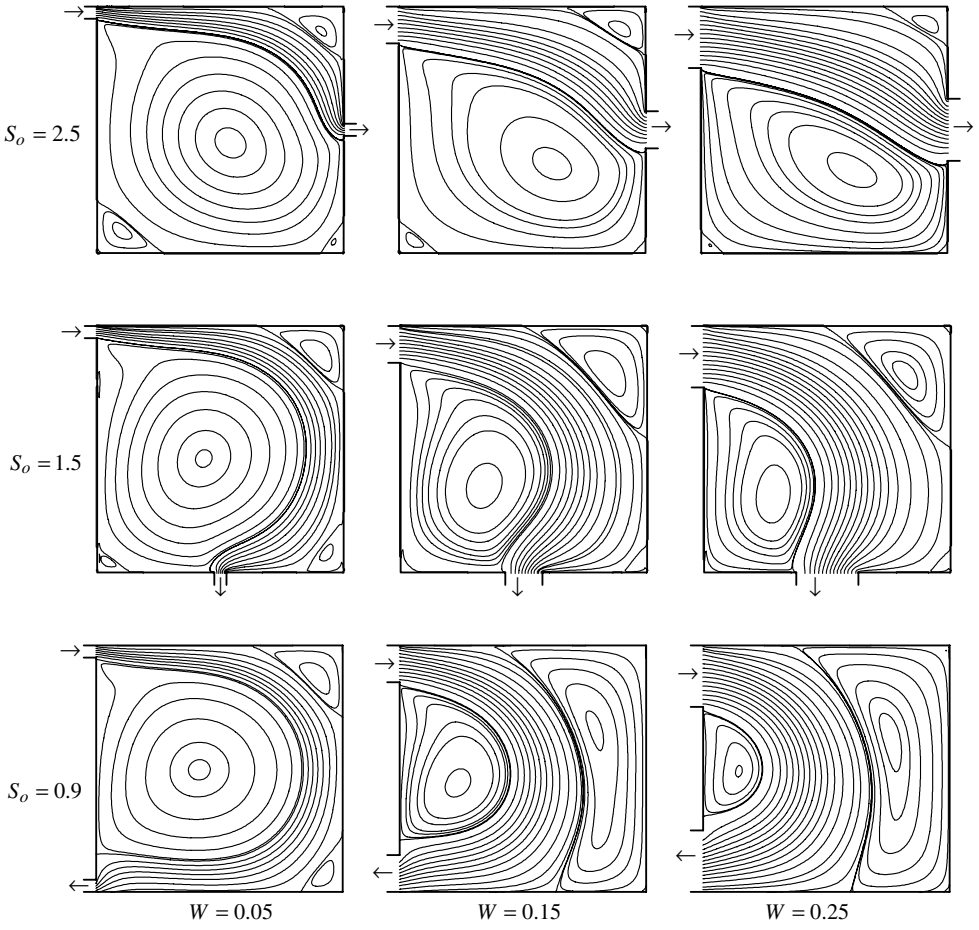

Fig. 5. Streamlines for $Re = 100$ with three outlet ports of widths $W = 0.05$, 0.15 and 0.25 positioned at three positions.

$Re = 10$ cases corresponding to these three outlet port positions, flow is generally void of vortices except for a small CCW rotating one at the top right corner and a CW rotating one at the bottom left corner. The flow fields shown in the bottom row of Fig. 3 are obtained as the outlet port is moved along the bottom wall to the left corner, with the bottom right corner case showing a situation where the two inlet and outlet ports are present on the left wall. As the outlet port is moved to the left, the primary CW vortex is found to shrink in size and occupies the space adjacent to the left wall. The CCW rotating vortex at the top right corner gains prominence as the outlet port is moved to the left side occupying the right half of the cavity in the most extreme case. An interesting feature of this CCW rotating vortex is its double-extrema property when the outlet port is located at $S_o = 1.5$. Similar trends were observed for other cases when the Reynolds number was lowered.

The effects of the position and width of the outlet ports on the flow field for $Re = 100$ are illustrated in Fig. 5. Going across each row, the width of the ports is varied whereas its location is fixed. Keeping everything else fixed, as the width of the ports increases, the size of the CW rotating primary vortex shrinks dramatically. For the top two rows with $S_o = 2.5$ and $S_o = 1.5$, as the width of the ports increases, the CCW vortices of the bottom left corner vanish and a CCW vortex gains prominence at the top right corner. Going across the bottom row of Fig. 5 that shows cases with both ports on the left wall, it is observed that the two CCW rotating vortices at the two corners of the right wall coalesce as the width of the port is increased.

The effect of the Reynolds number on the flow pattern is elucidated in Fig. 6 for two position and width combinations of the outlet port, i.e., (a) $W = 0.15$ and $S_o = 0.925$, and (b) $W = 0.25$ and $S_o = 1.5$. When the two ports are positioned on the left wall with $W = 0.15$ (Fig. 6a), the rise

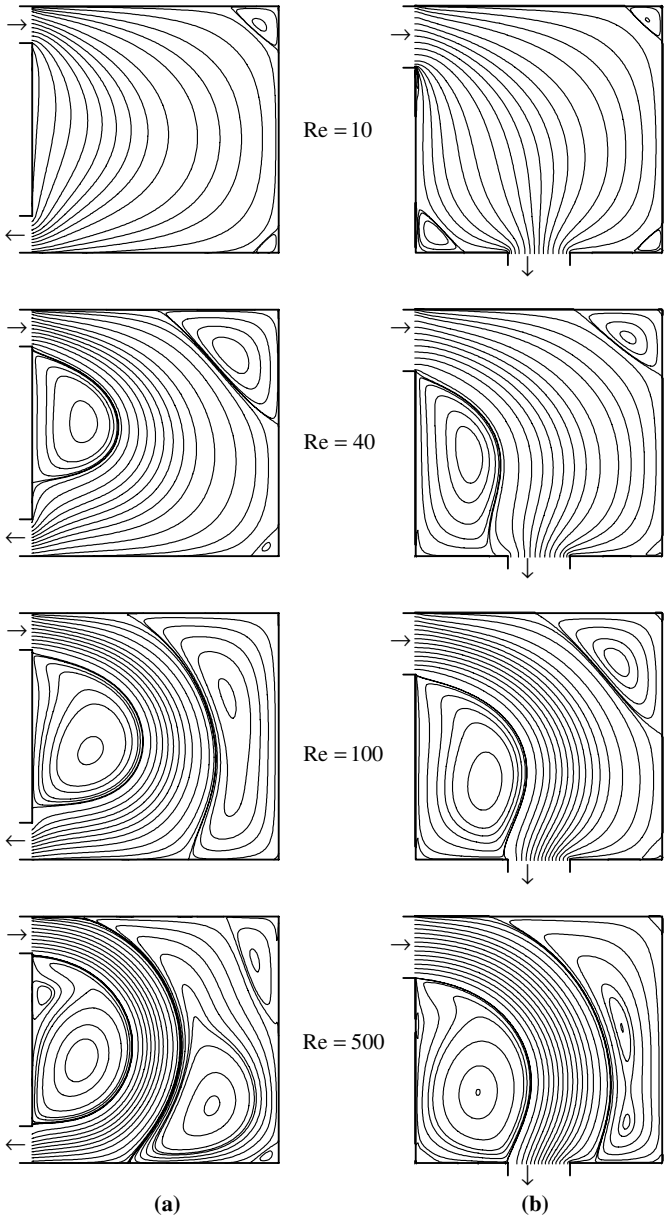

Fig. 6. Streamlines for (a) $W = 0.15$ and $S_o = 0.925$, and (b) $W = 0.25$ and $S_o = 0.15$, for Reynolds numbers of 10, 40, 100 and 500.

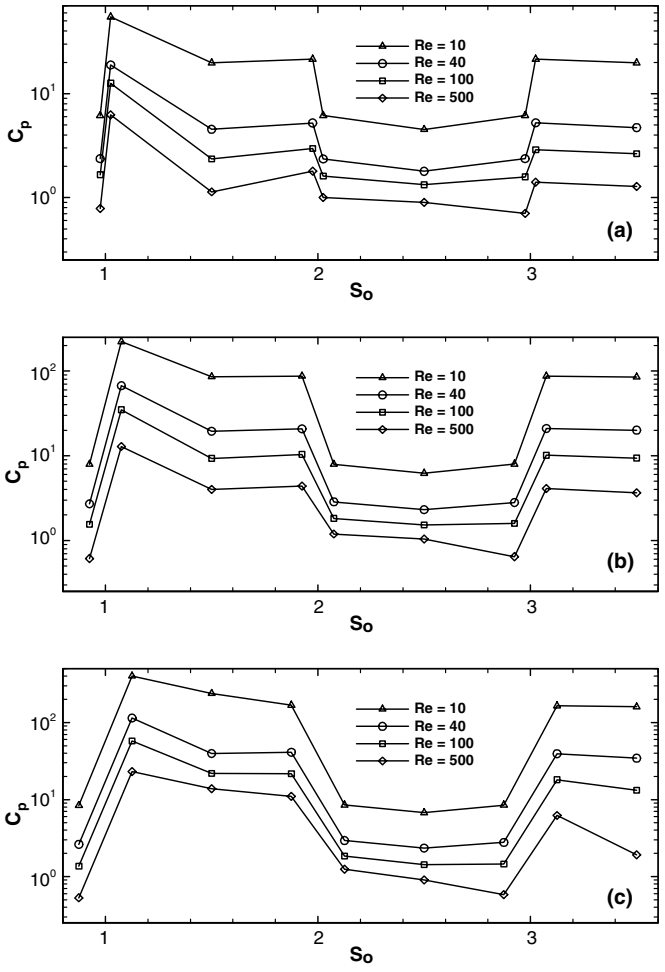

Fig. 7. Variations of the dimensionless pressure drop of the cavity for different positions of the outlet port with: (a) $W = 0.05$, (b) $W = 0.15$ and (c) $W = 0.25$ [Reynolds numbers are (△) 10, (○) 40, (□) 100 and (◇) 500].

in the value of the Reynolds number brings about a more complicated flow field with the number of CW and CCW vortices rising. As many as five vortices coexist for the $Re = 500$ case. The change in the number of vortices for the cases with the outlet at the middle of the bottom wall (Fig. 6b) is not observed, however the strength of the two existing vortices increases as Re is raised.

3.2. Pressure drop in the cavity

The pressure drop of the cavity is an important parameter in the design of microfilters [18] and piezoelectric microvalves [19]. The dimensionless pressure drop is related to the difference between the average pressures of the inlet and outlet ports by the following equation:

$$C_p = \frac{\bar{p}_{\text{in}} - \bar{p}_{\text{out}}}{1/2\rho u_{\text{in}}^2}. \tag{7}$$

The average pressures are calculated by integrating the pressure over the inlet and outlet ports as follows:

$$\bar{p}_{\text{in}} = \frac{\int_0^{w_{\text{i}}} p_{\text{in}}\,\mathrm{d}l}{w_{\text{i}}} \quad \text{and} \quad \bar{p}_{\text{out}} = \frac{\int_0^{w_{\text{o}}} p_{\text{out}}\,\mathrm{d}l}{w_{\text{o}}}. \tag{8}$$

The trapezoidal rule of numerical integration was used to evaluate the above integrals. In Fig. 7, the variation of the dimensionless pressure drop versus the position of the outlet port (S_{o}) for different Re numbers and widths of ports is shown. The pressure drop is a strong function of the position of the outlet port. For the cases that the outlet port is on the opposite or the same wall as the inlet port, the pressure drop is smaller in comparison to cases where it is located on the adjacent walls (i.e., top and bottom). This drastic change is illustrated clearly where the position of the outlet port changes from the end of a vertical wall to a position at the beginning of a horizontal wall and vise versa. But as it is seen in Fig. 7, the pressure drop does not alter markedly as the position of the outlet port changes on the same wall. The dimensionless pressure drop attains its maximum value with the outlet port located at the left side of the bottom wall, whereas for most cases it gains the minimum value with the outlet port at the middle of the right wall. For a couple of cases, the minimum is exhibited when the outlet port is at the bottom of the left wall or the top of the right wall, although the values for these three positions are very close to each other. It is also concluded that the pressure drop is increasing with the increase of port's width but is not a strong function of it. For design considerations, a low-leakage valve is realized with the highest pressure drop coefficient for a given flowrate (or Reynolds number). In the present configuration, such

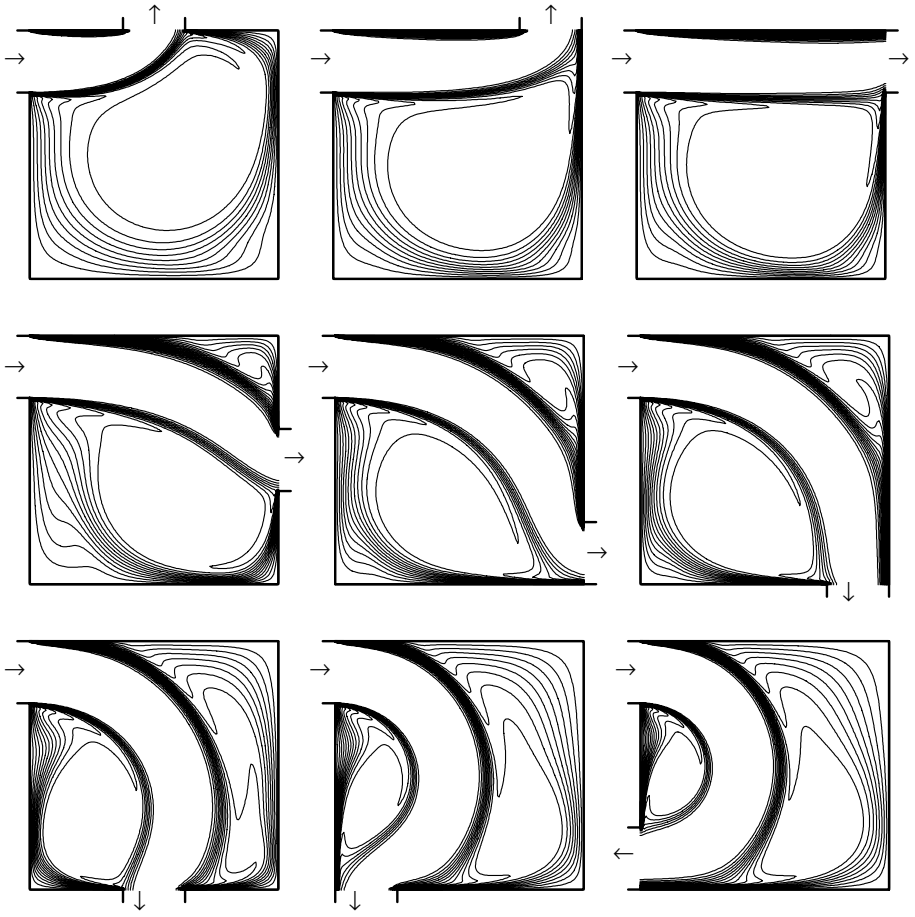

Fig. 8. Temperature fields for $Re = 500$ and $W = 0.25$ for nine different positions of the outlet port [contour level increment of 0.05].

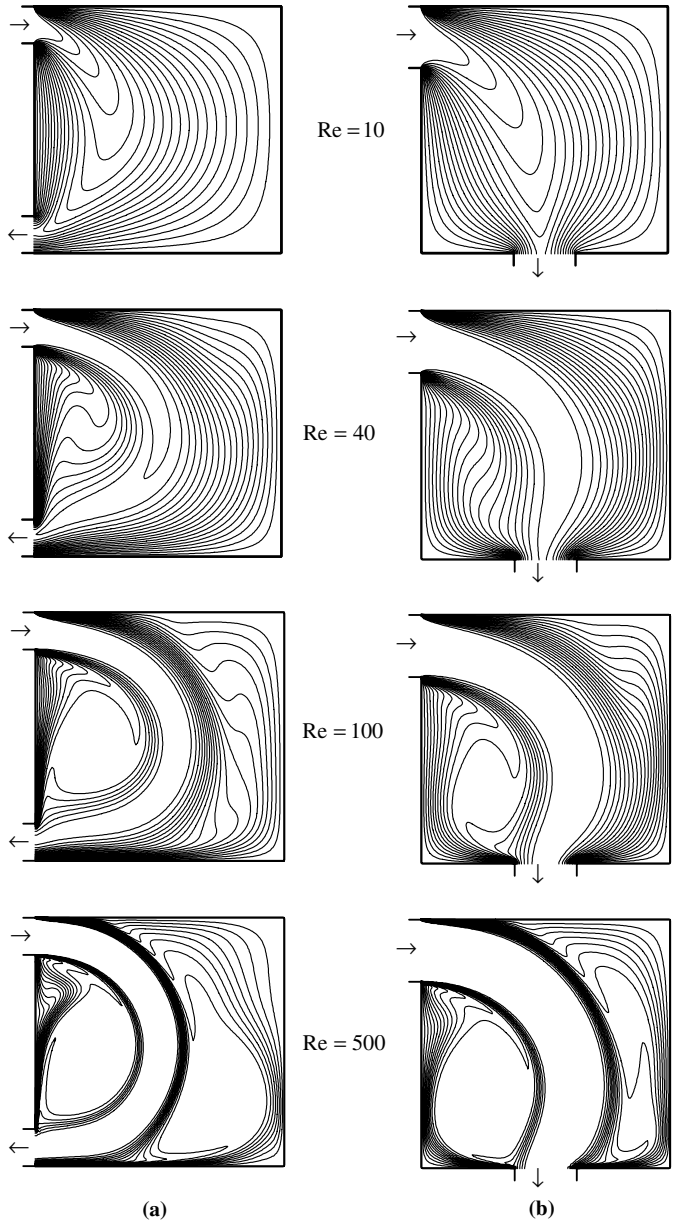

Fig. 9. Temperature fields for (a) $W = 0.15$ and $S_o = 0.925$, and (b) $W = 0.25$ and $S_o = 0.15$, for Reynolds numbers of 10, 40, 100 and 500 [contour level increment of 0.05].

an objective is realized with both ports placed on the same wall.

3.3. Temperature fields in the cavity

The contours of dimensionless temperature (θ) corresponding to nine cases with $Re = 500$ and $W = 0.25$ are shown in Fig. 8 for different positions of the outlet port. There is a one-to-one correspondence between each cavity in this figure to those shown in Fig. 3. In effect, the influence of the complicated flow field on the temperature field can be elucidated. The value of θ on the four solid walls is 1, whereas the value of θ of the fluid entering the cavity is zero, and the contour levels are incremented by 0.05. For the cases shown in the top row, the fluid temperature adjacent to the left, bottom and lower part of the right walls exhibit moderate spatial variations. On the other hand, fluid temperature gradients are marked next to the top portion of the right wall and next to the top wall. The temperature gradient is always marked at the interface of the throughflow stream and the CW rotating primary vortex suggesting intense heat exchange from the fresh incoming fluid to the CW primary vortex. The core of the primary vortex is generally isothermal. As the location of the outlet port is varied in the clockwise direction, it is noted that the regions of intense fluid temperature gradients are found on both sides of the outlet port. Marked temperature gradients are also noted on both sides of the throughflow stream indicating intense heat exchange with the neighboring vortices.

The effect of the Reynolds number on the temperature field is highlighted in Fig. 9 for two position and width combinations of the outlet port, i.e., (a) $W = 0.15$ and $S_o = 0.925$, and (b) $W = 0.25$ and $S_o = 1.5$. The temperature fields shown in Fig. 9 have one-to-one correspondence to the flow fields shown in Fig. 6. When the two ports are positioned on the left wall with $W = 0.15$, the rise in the value of the Reynolds number brings about steeper fluid temperature gradients next to the left and bottom walls, in addition to greater heat exchange on both sides of the throughflow. With the outlet at the middle of the bottom wall, the temperature gradient adjacent to the right wall is also seen to be enhanced as the Reynolds number is raised.

3.4. Variation of the local Nusselt number on the walls of the cavity

In order to evaluate the heat transfer rate along the walls, it is necessary to observe the variations of the local Nusselt numbers on these walls. These are defined as

$$Nu_i = -\left.\frac{\partial\theta}{\partial n}\right|_{\text{wall}}, \tag{9}$$

with the subscript i representing b, l, r and t that correspond to the bottom, left, right and top walls, respectively. The normal direction to each wall ($\pm X$ or $\pm Y$) is symbolized with n. In order to present the local Nusselt number variations on the four walls simultaneously, the use of the S coordinate system was adopted. For example, variations of the Nu_l, Nu_b, Nu_r and Nu_t are plotted in graphical form for intervals $S = 0$–1, $S = 1$–2, $S = 2$–3 and $S = 3$–4, respectively. This corresponds to traversing the inner wall of the cavity in the counter-clockwise direction starting at the top left corner. Variations of the local Nusselt number on the four walls of the cavity for different positions of the outlet port with $Re = 500$ and $W = 0.25$ are shown in Fig. 10. In this figure, no data for the Nusselt number is shown for $S = 0$–0.25 that corresponds to the location of

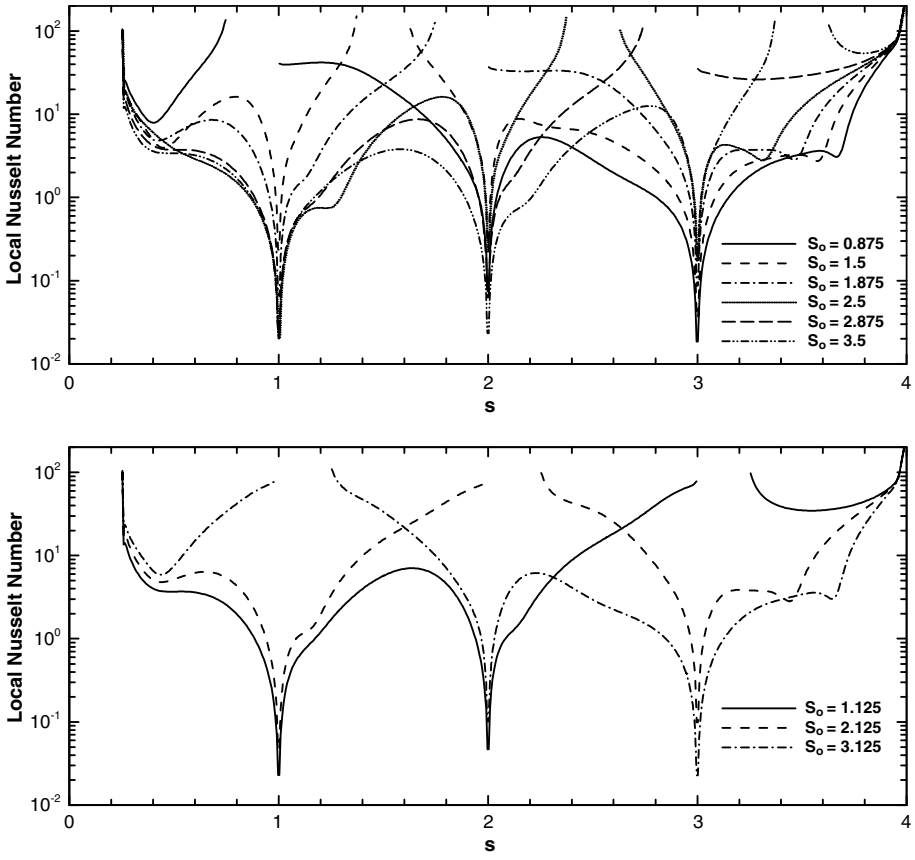

Fig. 10. Variations of the local Nusselt number on the four walls of the cavity for different positions of the outlet port with $Re = 500$ and $W = 0.25$.

the inlet port. Discontinuities for each individual curve correspond to changing location of the outlet port of the same width ($W = 0.25$). The Nusselt numbers shown in this figure correspond to the flow and temperature fields shown in Figs. 3 and 8, respectively, and therefore are directly affected by those complex variations. The three corners ($S = 1$, 2 and 3) that do not have outlet ports on either side exhibit very poor heat transfer rate due to their immediate proximity to small non-energetic vortices (Fig. 3) that are dominated by slow fluid motion. The two ends of the outlet port enjoy very intense heat transfer rate due to the steep temperature gradients already discussed in Fig. 8. In between these two extreme rates of heat transfer, the Nusselt number exhibits a variety of monotonic rise, monotonic decline, and far more complicated variations involving local minima and maxima points. These are directly dependent on the local status of the fluid temperature gradient on the walls that were previously shown in Fig. 8.

3.5. Variation of the overall Nusselt number of the cavity

Another variable utilized to evaluate the heat transfer rate is the overall or total Nusselt number of the cavity. Since all the four walls are active in heat exchange, the total Nusselt number is the sum of the individual mean Nusselt numbers, $\overline{Nu}_i$. Therefore, the total Nusselt number is defined as

$$\overline{Nu}_{\text{tot}} = \frac{1}{4}\sum_i \overline{Nu}_i = \frac{1}{4}\sum_i \frac{\int_{S_{i1}}^{S_{i2}} Nu_i \, \mathrm{d}S}{(S_{i2} - S_{i1})}, \tag{10}$$

with S_{i1} and S_{i2} being the S-coordinates of the two ends of the ith wall. The total Nusselt number of the cavity as a function of the position of the outlet port for different Re numbers and widths are given in Fig. 11. The dependence of the total Nusselt numbers take form of monotonically rising and decaying, piecewise functions that exhibit local maxima when the outlet ports are positioned with one end at the three corners ($S = 1$, 2 and 3). Between the two outlet ports with one end at a corner, the one with a higher S_o coordinate consistently gives rise to a higher heat transfer rate. On the other hand, the local minima overall heat transfer of the cavity is achieved with the outlet port located at the middle of the walls ($S_o = 1.5$, 2.5 and 3.5). These important findings can be used in design of practical heat exchange devices. By considering Figs. 7 and 11, it is clear that the best heat exchange cavity is realized when the outlet port's position corresponds to dimensionless wall coordinate S being $(2 + 0.5W)$. This will accommodate both maximum heat transfer and minimum pressure drop of the cavity.

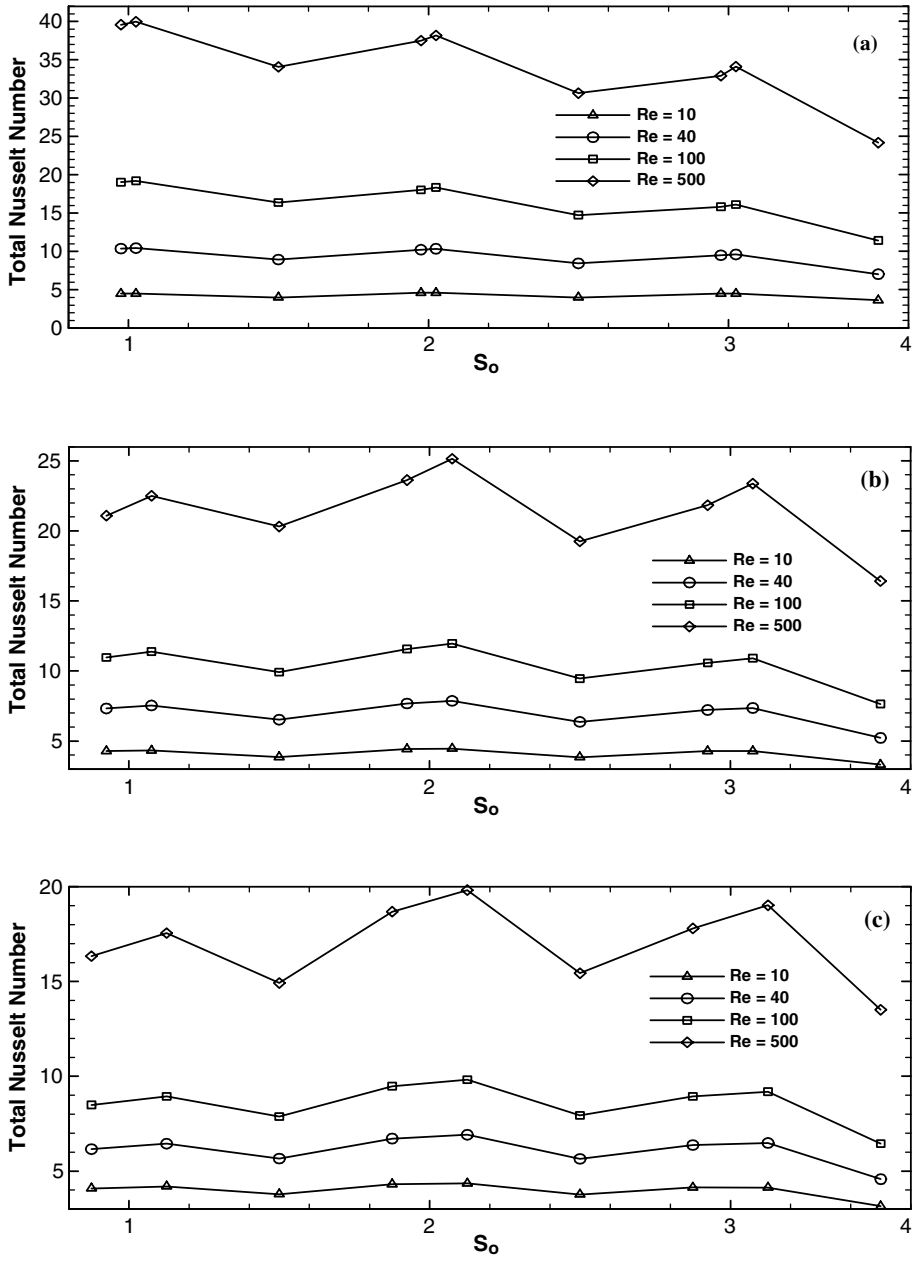

Fig. 11. Variations of the total Nusselt number of the cavity for different positions of the outlet port with different *Re* numbers: (a) $W = 0.05$, (b) $W = 0.15$ and (c) $W = 0.25$ [Reynolds numbers are (△) 10, (○) 40, (□) 100 and (◇) 500].

4. Conclusions

1. For high *Re* and with the shortest distance between the inlet and outlet ports along the top wall, a primary CW rotating vortex that covers about 75–88% of the cavity is observed. Similar cases with smaller *Re* exhibit identical flow patterns but with weaker vortices as *Re* is lowered. As the outlet port is moved along the right wall toward the bottom wall, the CW primary vortex diminishes in strength, however a CCW vortex that is present next to the top right corner covers a greater portion of the cavity. With the outlet port moving left along the bottom wall, the CW primary vortex is weakened further and the CCW vortex occupies nearly the right half of the cavity.
2. For design purposes, inlet and outlet ports should be parallel to each other in order to minimize pressure drop, even if they are designed to be placed on the same wall. In order to realize excessive pressure drops, it is recommended that they are perpendicular to each other. The distance between inlet and outlet ports and the width size of ports do not greatly affect the value of pressure drop.
3. The temperature fields are directly related to the presence of the multiple vortices in the cavity. Regions of high temperature gradient are consistently seen at the

interface of the throughflow with the neighboring vortices. Intense fluid temperature gradients are observed next to solid walls on both sides of the outlet port.

4. Local Nusselt numbers are low at three corners when no outlet port is present in their vicinity, whereas intense heat transfer rate is observed on the two sides of the outlet port. Between these minima and maxima points, the local Nusselt number can vary drastically depending on the flow and temperature fields adjacent to the respective wall.
5. By placing the outlet port with one end at three corners, maximum overall Nusselt number of the cavity can be achieved. Minimum overall heat transfer of the cavity is achieved with the outlet port located at the middle of the walls. The most effective location for the outlet port that accommodates maximum heat transfer and minimum pressure drop is when it is located at dimensionless wall coordinate equal to $(2 + 0.5W)$.

References

[1] X. Shi, J.M. Khodadadi, Laminar fluid flow and heat transfer in a lid-driven cavity due to a thin fin, J. Heat Transfer 124 (2002) 1056–1063.

[2] X. Shi, J.M. Khodadadi, Laminar natural convection heat transfer in a differentially heated square cavity due to a thin fin on the hot wall, J. Heat Transfer 125 (2003) 612–623.

[3] T.-H. Hsu, P.-T. Hsu, S.-P. How, Mixed convection in a partially divided rectangular enclosure, Numer. Heat Transfer, Part A 31 (1997) 655–683.

[4] T.H. Hsu, S.G. Wang, Mixed convection in a rectangular enclosure with discrete heat sources, Numer. Heat Transfer, Part A 38 (2000) 627–652.

[5] S.Z. Shuja, B.S. Yilbas, M.O. Iqbal, Mixed convection in a square cavity due to heat generating rectangular body. Effect of cavity exit port locations, Int. J. Numer. Methods Heat Fluid Flow 10 (2000) 824–841.

[6] S.Z. Shuja, B.S. Yilbas, M.O. Budair, Natural convection in a square cavity with a heat generating body: entropy considerations, Heat Mass Transfer 36 (2000) 343–350.

[7] A.M.C. Chan, P.S. Smereka, D. Giutsi, A numerical study of transient mixed convection flows in a thermal storage tank, J. Solar Energy Eng. 105 (1983) 246–253.

[8] A. Bouhdjar, A. Benkhelifa, A. Harhad, Numerical study of transient mixed convection in a cylindrical cavity, Numer. Heat Transfer, Part A 31 (1997) 305–324.

[9] K.O. Homan, S.L. Soo, The steady horizontal flow of a wall jet into a large-width cavity, J. Fluids Eng. 120 (1998) 70–75.

[10] A. Omri, S.B. Nasrallah, Control volume finite element numerical simulation of mixed convection in an air-cooled cavity, Numer. Heat Transfer, Part A 36 (1999) 615–637.

[11] G.M. Rosengarten, M. Behnia, G. Morrison, Some aspects concerning modelling the flow and heat transfer in horizontal mantle heat exchangers in solar water heaters, Int. J. Energy Res. 23 (1999) 1007–1016.

[12] A. Bouhdjar, A. Harhad, Numerical analysis of transient mixed convection flow in storage tank: influence of fluid properties and aspect ratios on stratification, Renew. Energy 25 (2002) 555–567.

[13] S. Singh, M.A.R. Sharif, Mixed convective cooling of a rectangular cavity with inlet and exit openings on differentially heated side walls, Numer. Heat Transfer, Part A 44 (2003) 233–253.

[14] J.M. Occhialini, J.J.L. Higdon, Convective mass transport from rectangular cavities in viscous flow, J. Electrochem. Soc. 139 (1992) 2845–2855.

[15] S. Jayaram, D. Thangaraj, Effects of eddies on convected space charge density in relaxation tanks, in: Proceedings of the Electrical/Electronics Insulation Conference, IEEE, 1995, pp. 123–127.

[16] L.C. Fang, D. Nicolaou, J.W. Cleaver, Transient removal of a contaminated fluid from a cavity, Int. J. Heat Fluid Flow 20 (1999) 605–613.

[17] P. Verboven, A.K. Datta, N.T. Anh, N. Scheerlinck, B.M. Nicolai, Computation of airflow effects on heat and mass transfer in a microwave oven, J. Food Eng. 59 (2003) 181–190.

[18] Y.-S. Leung Ki, D. Maillefer, G. Rey-Mermet, P.A. Monkewitz, P. Renaud, H.T.G. van Lintel, Microfluidics of a planar microfabricated fluid filter, Micro-ElectroMechanical Systems (MEMS)—1998, DSC-vol. 66, ASME, 1998, pp. 165–170.

[19] C. Lee, E.-H. Yang, S.M. Saeidi, J.M. Khodadadi, Fabrication, characterization and computational modeling of a piezoelectrically actuated microvalve for liquid flow control, J. Micro-ElectroMech. Syst. in press.

[20] S.M. Saeidi, Fluid flow and heat transfer in cavities with inlet and outlet ports: effect of flow oscillation and application to design of microvalves, Ph.D. Thesis, Department of Mechanical Engineering, Auburn University, 2005.

[21] S.V. Patankar, Numerical Heat Transfer and Fluid Flow, Hemisphere Pub. Co., Washington, DC, 1980.

[22] T. Hayase, J.A.C. Humphrey, R. Grief, A consistently formulated QUICK scheme for fast and stable convergence using finite-volume iterative calculation procedures, J. Comput. Phys. 98 (1992) 108–118.